

Article

Boosted Catalytic Performance of Ni₂Co₂@T-PMo@ZIF-67 for Glucose Oxidation in a Direct-Glucose Fuel Cell

Shipu Jiao ^{1,†}, Ning Kang ^{1,†}, Miao Liu ¹, Yihao Zhang ¹, Yang Li ¹, Bushra Maryam ¹ , Xu Zhang ¹, Pingping Zhang ^{2,*} and Xianhua Liu ^{1,*} 

¹ School of Environmental Science and Engineering, Tianjin University, Tianjin 300354, China; jsp@tju.edu.cn (S.J.); 2120214001@tju.edu.cn (N.K.); liumiao@tju.edu.cn (M.L.); zhangyihao_@tju.edu.cn (Y.Z.); liyang_@tju.edu.cn (Y.L.); maryambushra@yahoo.com (B.M.); zhangxu_2022@tju.edu.cn (X.Z.)

² College of Food Science and Engineering, Tianjin Agricultural University, Tianjin 300384, China

* Correspondence: zpp@tjau.edu.cn (P.Z.); lxh@tju.edu.cn (X.L.)

† These authors contributed equally to this work.

Abstract: In this study, we report on how to design efficient catalysts for glucose oxidation via the transitional metal doping of nanohybrids of polyoxometalates (POMs) and metal-organic frameworks (MOFs). ZIF-67, a cobalt-based MOF, as well as phosphomolybdic acid (PMo), were used as precursors for the fabrication of pyrolyzed PMo@ZIF-67 (T-PMo@ZIF-67). A different amount of Ni²⁺ was doped into PMo@ZIF-67 to produce Ni_xCo_y@T-PMo@ZIF-67. Among them, Ni₂Co₂@T-PMo@ZIF-67 had the best performance. The power density of the fuel cell that used Ni₂Co₂@T-PMo@ZIF-67 as an anode catalyst was 3.76 times that of the cell that used active carbon as an anode catalyst. SEM and EDS mapping results indicate that Ni₂Co₂@T-PMo@ZIF-67 has a spherical structure and rough surface, and elements such as cobalt, nickel, and molybdenum are evenly distributed. XRD characterization indicates that Co₃O₄, CoMoO₄, CoNiO₄, and MoNiO₄ co-exist in the composites. It is supposed that Co²⁺, Mo⁶⁺, and Ni²⁺ in the composites may have synergistic effects on the catalytic oxidation of glucose.

Keywords: MOF derivatives; polyoxometalates; fuel cells; catalysis



Citation: Jiao, S.; Kang, N.; Liu, M.; Zhang, Y.; Li, Y.; Maryam, B.; Zhang, X.; Zhang, P.; Liu, X. Boosted Catalytic Performance of Ni₂Co₂@T-PMo@ZIF-67 for Glucose Oxidation in a Direct-Glucose Fuel Cell. *Catalysts* **2024**, *14*, 19. <https://doi.org/10.3390/catal14010019>

Academic Editors: Piotr Bartczak, Jaroslaw Polanski and Tomasz Studyga

Received: 11 October 2023

Revised: 21 December 2023

Accepted: 24 December 2023

Published: 27 December 2023



Copyright: © 2023 by the authors. Licensee MDPI, Basel, Switzerland. This article is an open access article distributed under the terms and conditions of the Creative Commons Attribution (CC BY) license (<https://creativecommons.org/licenses/by/4.0/>).

1. Introduction

Metal-organic frameworks (MOFs) are a class of crystalline porous materials with a periodic network structure formed by interconnecting inorganic metal centers (metal ions or metal clusters) with bridging organic ligands through self-assembly. In MOFs, the organic ligands, as well as metal ions or clusters, are arranged with an obvious orientation, which can form different framework pore structures, thus exhibiting different adsorption properties, optical properties, electromagnetic properties, catalytic properties, etc. [1,2]. The preparation of MOF-derived materials performed via pyrolysis using metal-organic framework materials (MOFs) as templates, or precursors, has become a popular method for catalyst development [3–6]. The integration of MOFs into various materials, such as metal nanoparticles and semiconductors, can further improve the performance of MOF derivatives, but the selection of specific metal precursors and MOFs ligands is very limited, so the obtained functional materials do not meet the increasing needs of diverse applications [7]. Polyoxometalate (POM) is a negatively charged transition metal ion aggregate formed in a high oxygen state, and has a special and superior three-dimensional structure, as well as physical and chemical properties [8–10]. The structure, surface chemistry, polarity, charge, and redox properties of POMs can be easily tailored by the introduction of organic moieties and metal-organic groups. However, their electrochemical applications are limited due to their moderate electrochemical performance and low specific surface area. MOFs have the advantages of high porosity, large specific surface area, good chemical stability, and multiple adsorption sites. They can enclose POMs in their metal-organic skeleton so

as to avoid the loss of POMs and prolong the catalyst service life [11,12]. Therefore, the combination of MOFs and POMs is expected to expand the availability of transition metal elements, as well as improve the performance of MOF-derived materials [13–17].

With the gradual depletion of fossil resources, and the aggravated environmental deterioration, the development of novel technologies for sustainable energy conversion and storage has attracted global attention [18–21]. Glucose fuel cells (GFC) are one type of fuel cells that produce electricity by oxidizing glucose at the anode and reducing oxygen at the cathode. Glucose is the most abundant monosaccharide in nature, and is cheap and easy to obtain, non-volatile, and safe. It is also environmentally friendly, green, and non-toxic [22]. Glucose fuel cells can be divided into two categories according to the operating environment: external fuel cells and implantable fuel cells. In the case of external operation, glucose fuel cells can directly use agricultural waste as an energy source for power generation, which has the advantages of simplicity, safety, environmental protection, and wide fuel sources. Implantable fuel cells use glucose in body fluids, such as interstitial fluid, tears, blood, and cerebrospinal fluid to power the corresponding implanted devices. They have broad application prospects in implantable medical devices such as cardiac pacemakers and drug delivery pumps [23,24]. Generally, glucose is harder to oxidize than conventional substrates of fuel cells such as hydrogen and methanol, and thus needs an efficient and selective catalyst [25,26]. The anodic glucose oxidation reaction is slow, and the substrate is difficult to react completely [27,28]. The catalyst can improve the anodic oxidation rate of glucose fuel cells [29–32]. Currently, Pt is considered to be the most efficient catalyst for various fuel cells, but high Pt loading are required to meet practical applications [33,34]. As a result, fuel cells are too expensive to be commercialized on a large scale. It is a great challenge to develop high performance and low-cost anode catalysts for GFCs [35].

In this paper, we used phosphomolybdic acid (PMo, a keggin-type POM), as well as ZIF-67 (a cobalt-based MOF), as precursors for the fabrication of pyrolyzed PMo@ZIF-67 (T-PMo@ZIF-67). We tried to enhance their catalytic performance by doping various transitional metal ions (Ni^{2+} , Fe^{3+} , Cu^{2+} , and Zn^{2+}) in the preparation process of T-PMo@ZIF-67. The effects of doping with different transitional metal ions on the electrochemical performance were investigated. In addition, the possible mechanism of glucose oxidation under an alkaline environment was also discussed.

2. Results and Discussion

2.1. Electrochemical Performance Characterization of Anodic Catalysts

2.1.1. Linear Sweep Voltammetry (LSV) Measurement

Figure 1a shows the LSV plots of the different T-XPMo@ZIF-67 anodes, where the current density of T-NiPMo@ZIF-67 was always higher than that of T-PMo@ZIF-67. The current density of T-CuPMo@ZIF-67 and T-FePMo@ZIF-67 were lower than that of T-PMo@ZIF-67 at the same potential, and the current density of T-ZnPMo@ZIF-67 was even lower than the blank control anode (AC) at the potential range of -0.46 V~ 0.3 V. The oxidation current increased in the order of T-ZnPMo@ZIF-67 < AC < T-FePMo@ZIF-67 < T-CuPMo@ZIF-67 < T-PMo@ZIF-67 < T-NiPMo@ZIF-67. This indicates that Zn^{2+} remarkably impairs the catalytic activity of T-PMo@ZIF-67. It can be inferred that Zn^{2+} has a lower catalytic activity towards glucose oxidation. The addition of Zn^{2+} may precede the formation of ZIF-8 material by Co^{2+} during the preparation process, resulting in the loss of Co^{2+} during the preparation process and the reduction of Co^{2+} involved in the reaction. Although Cu^{2+} and Fe^{2+} can promote the glucose oxidation reaction, the catalytic performances of T-CuPMo@ZIF-67 and T-FePMo@ZIF-67 were not as high as that of T-PMo@ZIF-67. The doping of Ni^{2+} in the catalyst significantly increased the oxidation current of the glucose.

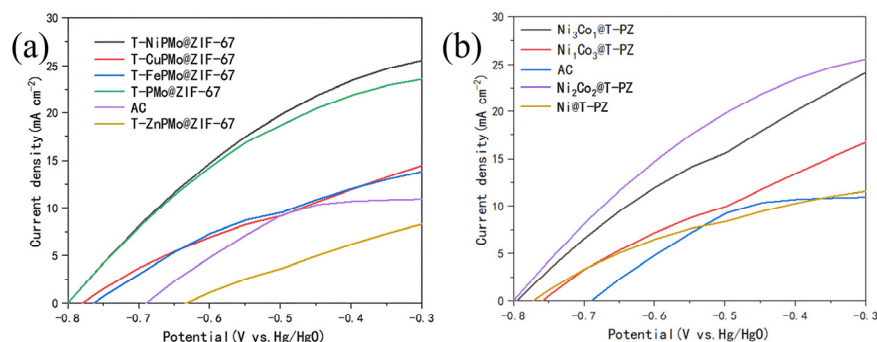


Figure 1. (a) LSV diagram of T-XPmo@ZIF-67 doped anodes; (b) LSV diagram of Ni_xCo_y@ZIF-67 doped anodes (10 mL 3 M of KOH and 1 M of glucose solution).

In order to optimize the catalytic performance of T-NiPMo@ZIF-67, the Co²⁺/Ni²⁺ ratio was tailored in the synthesis process of Ni_xCo_y@T-PZ. Figure 1b shows the LSV measurements of the catalysts with different Co²⁺/Ni²⁺ ratios. The current densities of the four anodes were higher than that of the AC control, and the maximum current density was increased in the order of AC < Ni@T-PZ < Ni₁Co₃@T-PZ < Ni₃Co₁@T-PZ < Ni₂Co₂@T-PZ. This result further confirmed that doping with appropriate amounts of Ni²⁺ (1.25 mM) can promote the oxidation of glucose, and the optimal Co²⁺/Ni²⁺ ratio as a molar ratio was 1:1. Co²⁺ and Ni²⁺ may have a synergistic effect on the catalytic oxidation capacity of glucose. Therefore, the LSV curves of Ni₃Co₁@T-PZ and Ni₂Co₂@T-PZ were higher than that of Ni@T-PZ, which Ni²⁺ was added alone. However, when the concentration of either metal ion was higher, the catalytic performance of the catalyst would deteriorate.

2.1.2. Electrochemical Impedance Testing (EIS) of Anodes

EIS tests were performed on anodes modified with different catalysts. The resulting data were fitted by the equivalent circuit diagram (Figure S1). Figure 2a shows the EIS curves corresponding to blank anodes (AC), T-PMo@ZIF-67, T-NiPMo@ZIF-67, T-CuPMo@ZIF-67, T-FePMo@ZIF-67, and T-ZnPMo@ZIF-67 catalyst doped anodes. Table 1 shows the impedance values of each part of the anode modified by different anode catalysts. As can be seen from the figure, the performance of T-NiPMo@ZIF-67 was significantly better than that of blank AC anode and other metal ion catalysts, showing the smallest Ohmic resistance and charge transfer resistance. The difference between the several electrodes was that the metal ions added were different, which indicates that the type of metal ions has an important effect on the conductivity of the electrode surface.

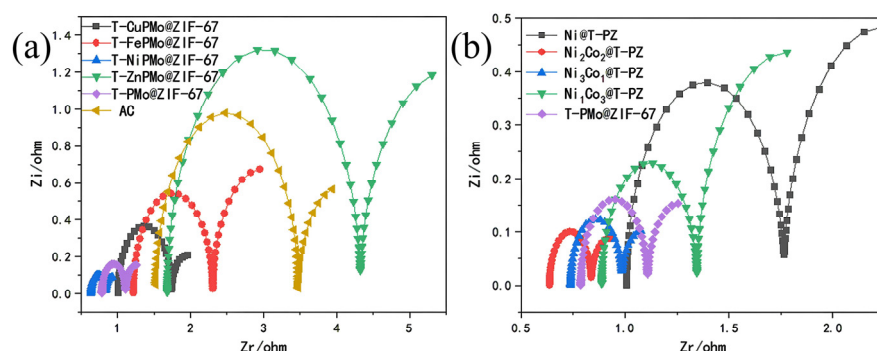


Figure 2. (a) EIS diagram of the different T-XPmo@ZIF-67 anodes; (b) EIS diagram of the Ni_xCo_y@T-PZ anodes (10 mL 3 M of KOH and 1 M of glucose solution).

In order to better study the effects of Co²⁺/Ni²⁺ ratio on the performance of T-NiPMo@ZIF-67, the impedance of the anodes with different Co²⁺/Ni²⁺ ratios were analyzed. Figure 2b and Table 2 show the Rct was increased in the order of Ni₂Co₂@T-PZ < Ni₃Co₁@T-PZ < T-PMo@ZIF-67 < Ni₁Co₃@T-PZ < Ni@T-PZ. As can be seen from Table 2,

changes of R_s of the anodes with different $\text{Co}^{2+}/\text{Ni}^{2+}$ ratios were consistent with R_{ct} . $\text{Ni}_2\text{Co}_2@T\text{-PZ}$ had the smallest R_s of 0.686 Ω . The R_{ct} of $\text{Ni}_2\text{Co}_2@T\text{-PZ}$ (0.1755 Ω) was decreased by 42.70% when compared with $T\text{-PMo}@ZIF\text{-67}$ (0.3063 Ω), and decreased by 76.85% when compared with $\text{Ni}@T\text{-PZ}$ (0.7582 Ω). Compared with $T\text{-PMo}@ZIF\text{-67}$ and $\text{Ni}@T\text{-PZ}$, the total resistance of $\text{Ni}_2\text{Co}_2@T\text{-PZ}$ decreased by 24.88% and 61.10%, respectively. These data can explain why the performance of $\text{Ni}_2\text{Co}_2@T\text{-PZ}$ is better than that of other catalysts. The decrease of transfer resistance accelerated the electron transfer and improved the current flow.

Table 1. Impedance values of $T\text{-XPMo}@ZIF\text{-67}$ anodes.

	AC	T-CuPMo@ZIF-67	T-FePMo@ZIF-67	T-NiPMo@ZIF-67	T-ZnPMo@ZIF-67	T-PMo@ZIF-67
R_s (Ω)	1.518	1.002	1.162	0.686	1.68	0.7869
R_{ct} (Ω)	1.151	0.4188	0.6594	0.1755	2.643	0.3063
R_d (Ω)	1.957	0.7333	0.7416	0.201	2.403	0.3212
R_t (Ω)	4.626	2.1541	2.563	1.0625	6.726	1.4144

Table 2. Impedance values of $\text{Ni}_x\text{Co}_y@T\text{-PZ}$ anodes.

	Ni@T-PZ	$\text{Ni}_1\text{Co}_3@T\text{-PZ}$	$\text{Ni}_3\text{Co}_1@T\text{-PZ}$	$\text{Ni}_2\text{Co}_2@T\text{-PZ}$	T-PMo@ZIF-67
R_s (Ω)	1.006	0.887	0.738	0.686	0.7869
R_{ct} (Ω)	0.7582	0.4577	0.202	0.1755	0.3063
R_d (Ω)	0.967	0.8711	0.2467	0.201	0.3212
R_t (Ω)	2.7312	2.2158	1.1867	1.0625	1.4144

2.1.3. The Tafel Curve of Anodes

The Tafel curve is a section of the strong polarization region of the general polarization curve. For the simpler electron transfer process, the Tafel curve can be used for analysis, and the exchange current density can be obtained through using the linear part of the Tafel curve to intersect the axis through the extension line, so as to calculate the number of electrons transferred in the electrochemical process. Figure 3a shows the Tafel curve of different catalyst modified anodes, and Figure 3b shows the fitting curves. Table 3 shows the fitting results of the Tafel measurement. As can be seen from Figure 3b and Table 3, The Tafel slopes of AC, $T\text{-PMo}@ZIF\text{-67}$, $\text{Ni}@T\text{-PZ}$, $\text{Ni}_3\text{Co}_1@T\text{-PZ}$, $\text{Ni}_2\text{Co}_2@T\text{-PZ}$, and $\text{Ni}_1\text{Co}_3@T\text{-PZ}$ were 186.1702, 207.3794, 184.5195, 197.7402, 194.4443 and 191.6377 mV dec^{-1} respectively. The I_0 of the different anodes were increased in the order of AC ($3.831 \times 10^{-4} \text{ A cm}^{-2}$) < $\text{Ni}@T\text{-PZ}$ ($8.283 \times 10^{-4} \text{ A cm}^{-2}$) < $\text{Ni}_1\text{Co}_3@T\text{-PZ}$ ($10.117 \times 10^{-4} \text{ A cm}^{-2}$) < $T\text{-PMo}@ZIF\text{-67}$ ($24.526 \times 10^{-4} \text{ A cm}^{-2}$) < $\text{Ni}_3\text{Co}_1@T\text{-PZ}$ ($34.901 \times 10^{-4} \text{ A cm}^{-2}$) < $\text{Ni}_2\text{Co}_2@T\text{-PZ}$ ($37.884 \times 10^{-4} \text{ A cm}^{-2}$). $\text{Ni}_2\text{Co}_2@T\text{-PZ}$ had the highest exchange current density, which was much higher than that of the AC anode. This indicates that the glucose oxidation reaction of $\text{Ni}_2\text{Co}_2@T\text{-PZ}$ catalyst doped anode can be carried out at a lower overpotential. It was confirmed that $\text{Ni}_2\text{Co}_2@T\text{-PZ}$ can significantly promote the oxidation of glucose, increase the reaction rate, and improve the performance of fuel cell.

Table 3. Tafel curve fitting results.

	Fitting Equation	R^2	Tafel (mV dec^{-1})	$10^{-4}I_0$ (A cm^{-2})
AC	$y = 5.37143 \times -3.41673$	0.9983	186.1702	3.831
$\text{Ni}@T\text{-PZ}$	$y = 5.41948 \times -3.08181$	0.99818	184.5195	8.283
$\text{Ni}_3\text{Co}_1@T\text{-PZ}$	$y = 5.05714 \times -2.45716$	0.99876	197.7402	34.901
$\text{Ni}_2\text{Co}_2@T\text{-PZ}$	$y = 5.14286 \times -2.42154$	0.99758	194.4443	37.884
$\text{Ni}_1\text{Co}_3@T\text{-PZ}$	$y = 5.21818 \times -2.99496$	0.99807	191.6377	10.117
$T\text{-PMo}@ZIF\text{-67}$	$y = 4.82208 \times -2.61037$	0.99766	207.3794	24.526

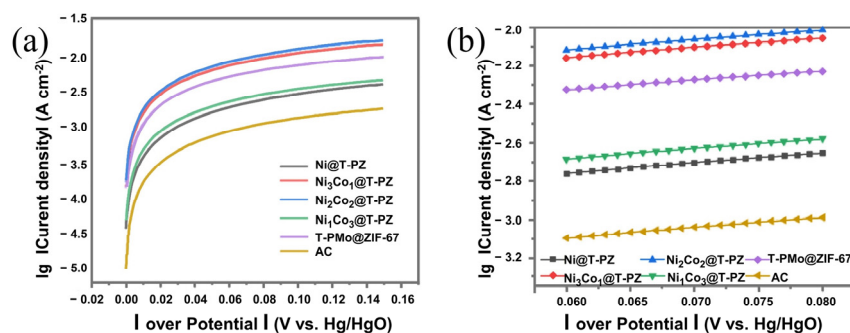


Figure 3. (a) Tafel curves of the $\text{Ni}_x\text{Co}_y\text{@T-PZ}$ anodes; (b) Tafel curve fitting results for different $\text{Ni}_x\text{Co}_y\text{@T-PZ}$ anodes (10 mL 3 M of KOH and 1 M of glucose solution).

2.1.4. Power Density (PD) and Polarization Curves (PC) of Different Anodes in Fuel Cells

In order to evaluate the performance of $\text{Ni}_2\text{Co}_2\text{@T-PZ}$ in real alkaline glucose fuel cells, a whole-cell investigation was conducted through using carbon fabric as the air cathode, and catalyst-modified active carbon as the anode. Figure 4a shows the power density curves of the fuel cell with the different catalyst-modified anodes. The power densities of the fuel cell had a similar change trend, rising at first and then declining. The maximum power densities of the fuel cell with different anodes increased in the order of AC (9.060 W m^{-2}) < Ni@T-PZ (19.567 W m^{-2}) < $\text{Ni}_1\text{Co}_3\text{@T-PZ}$ (21.515 W m^{-2}) < T-PMo@ZIF-67 (27.916 W m^{-2}) < $\text{Ni}_3\text{Co}_1\text{@T-PZ}$ (31.774 W m^{-2}) < $\text{Ni}_2\text{Co}_2\text{@T-PZ}$ (34.065 W m^{-2}). The power density of the fuel cell with $\text{Ni}_2\text{Co}_2\text{@T-PZ}$ as the anode catalyst was always higher than that of the others with the maximum power density of 34.065 W m^{-2} , which was 1.22 times of that with T-PMo@ZIF-67 anode, 1.74 times of that with Ni@T-PZ anode, and 3.76 times of that with AC anode. Compared to other glucose fuel cells, our work has advantages in terms of performance and cost (Table 4).

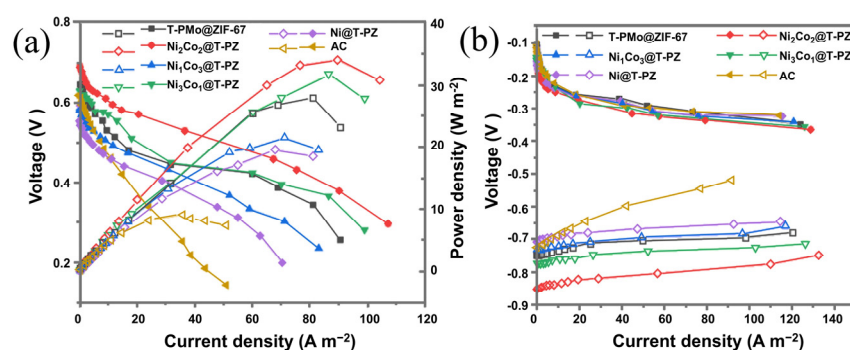


Figure 4. (a) Polarization and power density curves of the fuel cell equipped with different $\text{Ni}_x\text{Co}_y\text{@T-PZ}$ doped anodes (The blank sign represents the power density curves of alkaline glucose fuel cells constructed with air cathodes and different catalytic anodes, and the filled sign represents the current density and open circuit voltage of the alkaline glucose fuel cells.); (b) Individual cathode and anode polarization curves (10 mL 3 M of KOH and 1 M of glucose solution).

Table 4. Performance of glucose fuel cells with different electrodes and catalysts.

Anode	Cathode	Catalyst	Power Density	Reference
Ni	Al	Pt	$2 \mu\text{W cm}^{-2}$;	[36]
Pt	Pt	Pt	$43 \mu\text{W cm}^{-2}$;	[37]
PtPd/graphene	N-doped graphene oxide nanoribbons	Pt	$24.9 \mu\text{W cm}^{-2}$;	[38]
Nanoporous gold	Pt/C	Pt/Bi	8 mW cm^{-2} ;	[39]
Activated carbon/Ni-foam	Activated carbon/Ni-foam	$\text{Ni}_2\text{Co}_2\text{@T-PMo@ZIF-67}$	3.4 mW cm^{-2} ;	This work

Figure 4b shows the polarization curves of the different electrodes. Because all the systems use the same air cathode, the changes of total voltage and power density should be attributed to different anodes. Among the six anodes, the potential of the AC anode decreased the fastest. The potentials of Ni@T-PZ and Ni₁Co₃@T-PZ anodes had a mild decrease compared to that of the AC anode. Ni₂Co₂@T-PZ anode had the most robust performance. This result is consistent with the LSV, EIS, and Tafel measurements.

2.2. Characterization of T-PMo@ZIF-67

2.2.1. Scanning Electron Microscope Analysis

SEM characterization of the catalyst was used to observe the microstructure of Ni₂Co₂@T-PZ (Figure 5a). The diameter of Ni₂Co₂@T-PZ particle was about 200 nm. The element mapping for Ni₂Co₂@T-PZ showed that C, Co, Ni, Mo, O, and P were uniformly distributed throughout the structure, which proved the successful doping of Ni²⁺ in T-PMo@ZIF-67, and the distribution was uniform with no obvious agglomeration (Figure 5b). The energy dispersion spectra (EDS) of Ni₂Co₂@T-PZ catalyst indicated the molar ratio of Co, Mo, and Ni was 3.02:1:3.26 (Figure S2).

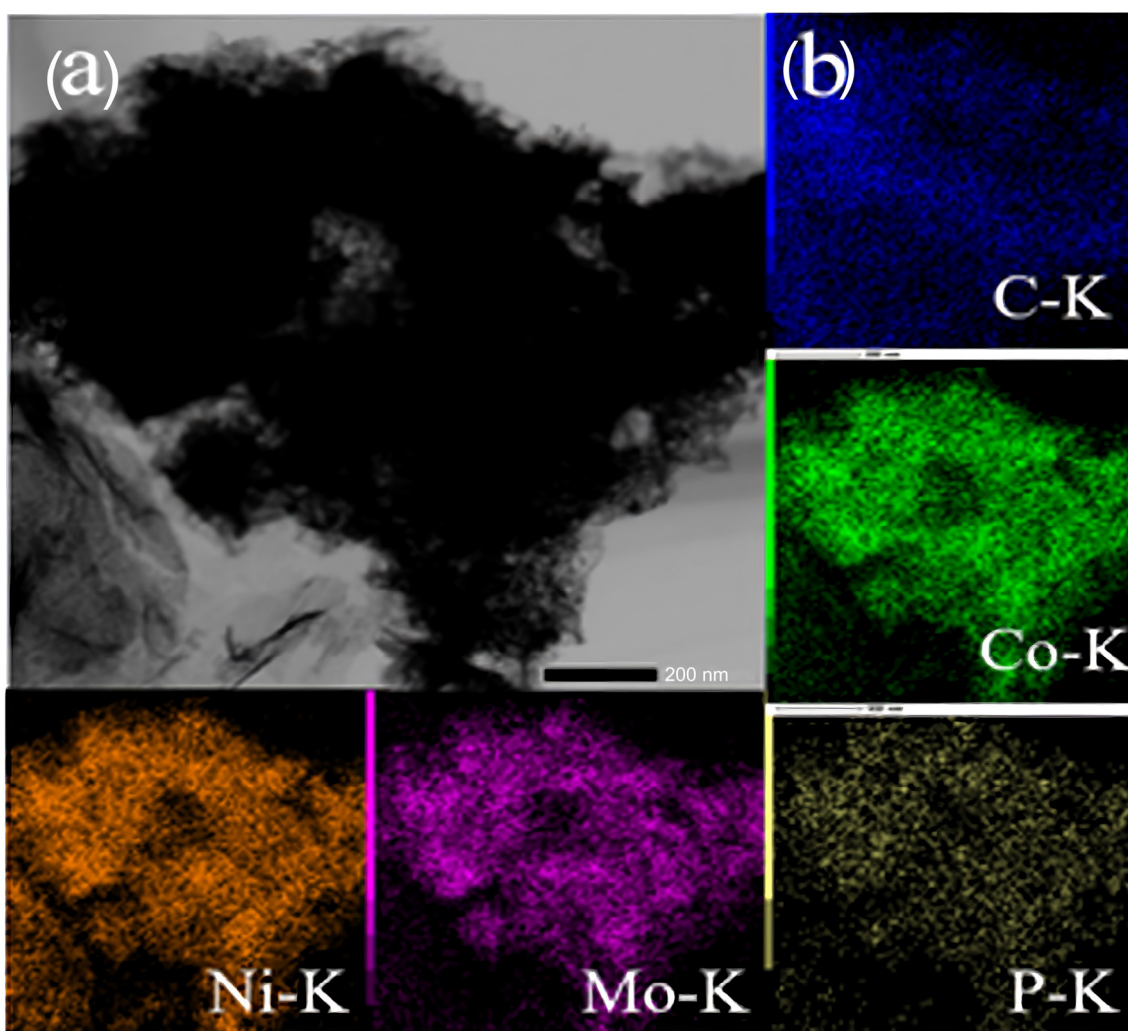


Figure 5. (a) SEM image of Ni₂Co₂@T-PZ. (b) Element diagram of Ni₂Co₂@T-PZ.

2.2.2. X-ray Diffraction Analysis

The XRD spectra of T-PMo@ZIF-67 and Ni₂Co₂@T-PZ (Figure 6) were compared, and the result showed that the peak size and peak area of the latter was remarkably increased, indicating a significant decrease in grain size. The presence of peaks at 36.6°, 43.3°, 45.2°, and 48.2° were observed.

and 50.6° represents the presence of CoNiO_4 and MoNiO_4 , which indicates that Ni^{2+} reacted with Co^{2+} and Mo^{2+} during the fabrication process. EDS and XRD results imply that Co_3O_4 , CoMoO_4 , CoNiO_4 , and MoNiO_4 coexist in $\text{Ni}_2\text{Co}_2\text{@T-PZ}$.

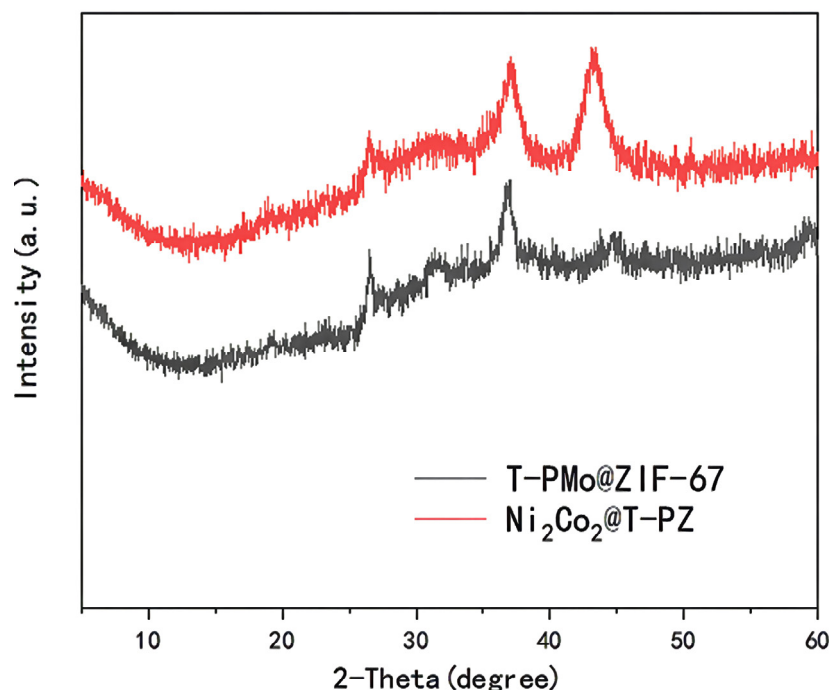


Figure 6. XRD pattern of T-PMo@ZIF-67 and $\text{Ni}_2\text{Co}_2\text{@ZIF-67}$.

2.2.3. X-ray Photoelectron Spectroscopy Analysis

The characterization of XPS is helpful when analyzing the elemental composition and valence distribution of $\text{Ni}_2\text{Co}_2\text{@T-PZ}$, so as to better understand the underlying catalytic mechanism. Figure 7a shows the XPS spectra of each element of $\text{Ni}_2\text{Co}_2\text{@T-PZ}$. The peaks centered at 855.10 eV, 796.06 eV, 530.14 eV, 284.95 eV, and 232.49 eV were Ni2p, Co2p, O1s, C1s, and Mo3d. The peaks centered at 284.77 eV, 286.28 eV, and 288.59 eV shown in Figure 7b represent C=C/C-C, C=C/C-C, and C=O for C1s signals. In Figure 7c, it can be seen there were two splitting slits at 235.34 eV and 232.22 eV in the XPS pattern of Mo3d, and the column width was 3.12 eV, which can be ascribed to Mo^{6+} . The spectrum of Co2p was mainly derived from the splitting of two orbitals, which were spin orbital double peaks with a column width of about 15 eV (Figure 7d). The spin orbital double peaks at 780 eV and 795 eV represented the $\text{Co}2p_{3/2}$ and $\text{Co}2p_{1/2}$ levels of the Co ion, respectively. The satellite peaks could be used to identify the oxidation state of Co ions. The energy gap between satellite peaks and the main peaks was 6 eV and 8 eV respectively, indicating that Co^{2+} and Co^{3+} co-exist in the sample. Figure 7e shows the XPS spectrum of Ni2p. The peaks at the binding energy of 853.97 eV and 860.98 eV was the characteristic peak of Ni^{3+} , and the double peak at the binding energy of 855.87 eV and 863.14 eV was the characteristic peak of Ni^{2+} . This result indicates that Ni^{3+} and Ni^{2+} coexist in the sample.

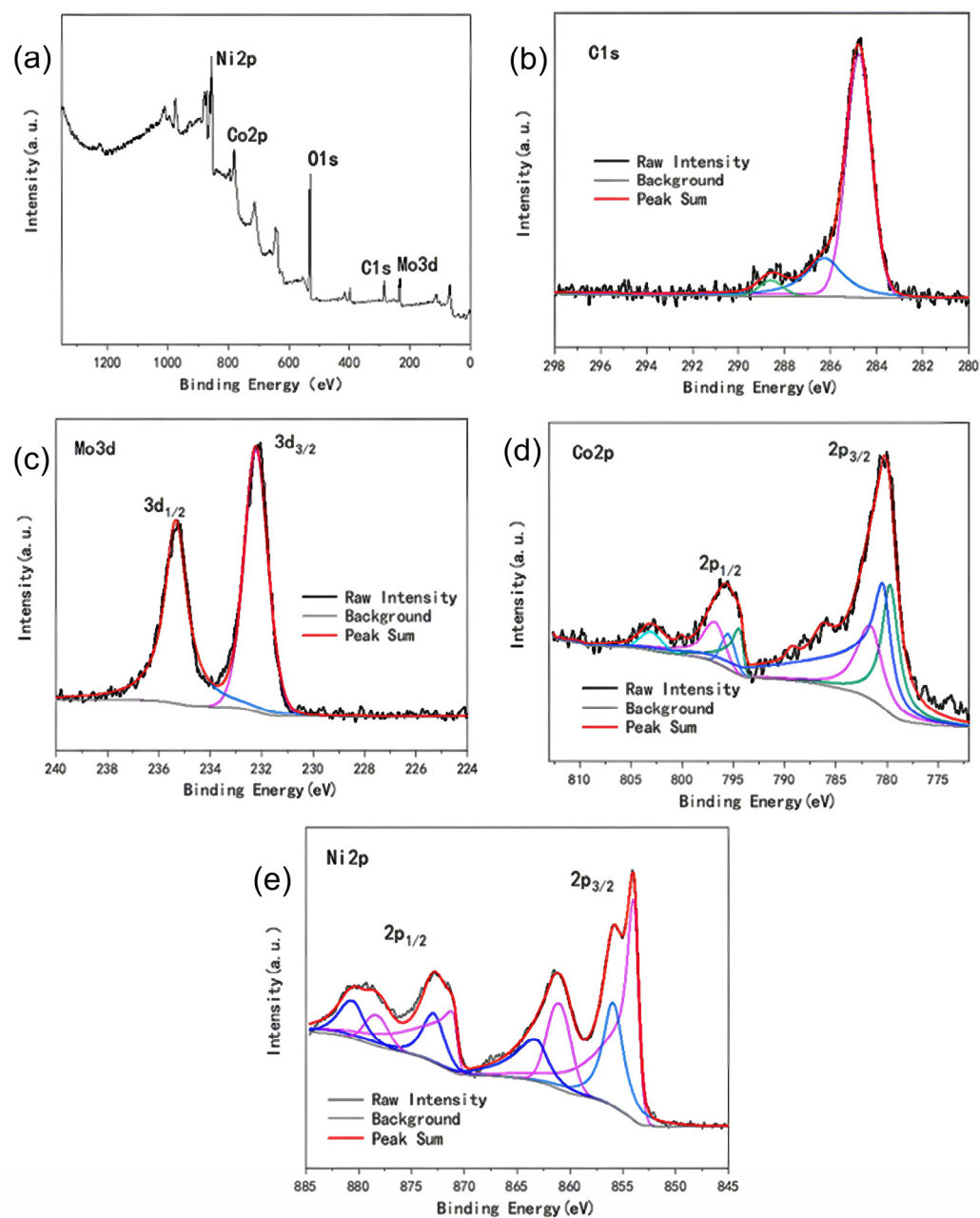
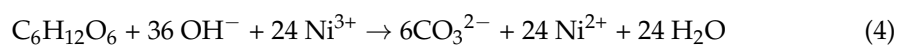
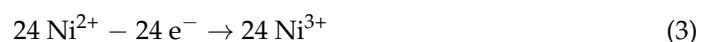
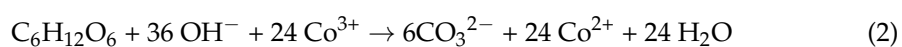
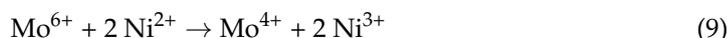
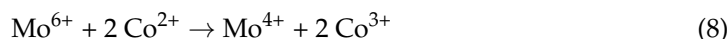
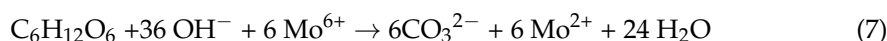


Figure 7. (a) Full spectrum of XPS for Ni₂Co₂@ZIF-67; (b) C 1s spectra; (c) Mo 3d spectra; (d) Co 2p spectra; (e) Ni 2p spectra.

2.3. Catalytic Mechanism

SEM, XPS, XRD, and electrochemical characterization results can be used to infer the catalytic mechanism of glucose oxidation by Ni₂Co₂@T-PZ in alkaline environment. The catalytic process can involve the following steps [40–45]:





Co^{3+} and Ni^{3+} generated from Co^{2+} and Ni^{2+} have a high oxidative state, which can accelerate the oxidation process of glucose under alkaline environment. Mo^{6+} has great tendency to acquire electrons from neighbor molecules. Firstly, it can react with Co^{2+} and Ni^{2+} to produce Co^{3+} and Ni^{3+} . In addition, it can directly capture electrons from glucose and be reduced to Mo^{2+} . Figure 8 depicts the possible reaction processes that $\text{Ni}_2\text{Co}_2\text{@T-PZ}$ involved in the oxidation of glucose. There may exist a synergistic effect between Co^{2+} , Ni^{2+} , and Mo^{6+} : with the good oxidizing property of Mo^{6+} , Co^{3+} , and Ni^{3+} being easily obtained, and Co^{3+} and Ni^{3+} being re-reduced to Co^{2+} and Ni^{2+} by oxidizing glucose. Meanwhile, there is a synergistic effect between reactions (1) and (3), Ni^{3+} has the ability to capture electrons from glucose, and Co^{2+} can play a facilitating role. The resulting Mo^{2+} is oxidized to Mo^{6+} via the cathodic transfer of electrons, resulting in catalyst recycling [46,47]. In addition, there is a good synergistic effect between POM and ZIF-67, so $\text{Ni}_2\text{Co}_2\text{@T-PZ}$ catalyst has a high specific surface area and abundant active sites, and also has excellent diffusion efficiency. The $\text{Ni}_2\text{Co}_2\text{@T-PZ}$ catalyst showed excellent catalytic performance for glucose oxidation [48,49].

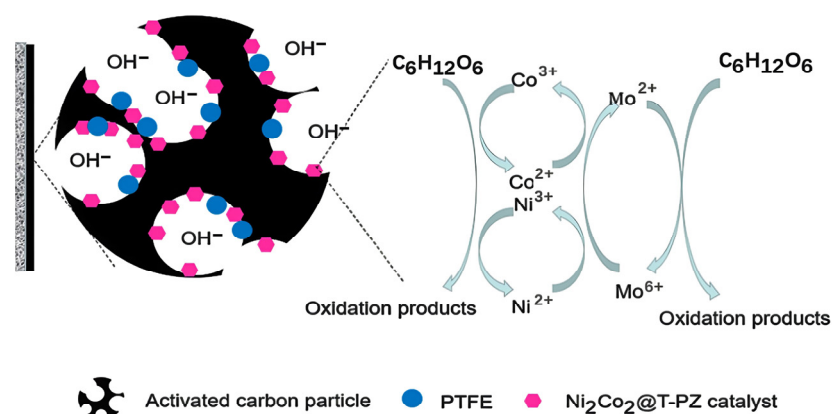


Figure 8. Mechanism diagram of $\text{Ni}_2\text{Co}_2\text{@T-PZ}$ catalyzed glucose oxidation.

3. Materials and Methods

3.1. Materials

Nickel foam was obtained from Yilongsheng Energy Technology Co., Ltd. (Suzhou, China). Activated Carbon (AC) powder (YEC-8A) was purchased from Yihuan Carbon Co., Ltd. (Fuzhou, China). A 60 wt% PTFE solution was purchased from Hesen Inc. (Shanghai, China). Phosphomolybdic acid hydrate (PMo12) and 2-methylimidazole were purchased from Kemiou (Tianjin, China). Glucose, KOH, and all the other chemicals were analytically pure. Deionized water (DI) was used as the solvent for all the solutions.

3.2. Characterization

Electrochemical characterization was carried out on a CHI-660E electrochemical workstation (Chenhua Instrument Co., Ltd., Shanghai, China). The microstructure of the samples was analyzed on a SEM (S4800, Hitachi High-tech Corporation, Tokyo, Japan) and a TEM (Tecnai G2 F20, IKA, Königswinter, Germany). X-ray diffraction (XRD) patterns were measured by a D/MX-III A X-ray diffractometer (Rigaku, Japan). XPS analysis was carried out on an Escalab 250Xi X-ray photoelectron spectrometer (Thermo Fisher Scientific, Waltham, MA, USA).

3.3. Preparation of Electrodes

3.3.1. Preparation of XPMo@ZIF-67 and Ni_xCo_y@PZ

An amount of 2.5 mM cobalt nitrate, together with 2.5 mM different transitional metal salts (copper nitrate, ferric nitrate, nickel nitrate or zinc nitrate), was added into 25 mL of methanol. After fully mixing, 10 mL of 30 mM phosphomolybdate aqueous solution was added into the bottle to obtain solution A (denoted as A1, A2, A3, and A4, respectively). Solution B was prepared by adding 20 mM 2-methylimidazole into 25 mL methanol. Solutions C was obtained by quickly mixing solution A with solution B (denoted as C1, C2, C3, and C4, respectively). Then, the mixture was heated in a hydrothermal reactor (10 h, 120 °C). Afterwards, purple precipitates were obtained. The obtained precipitates were filtered, and then were washed with ethyl alcohol. The precipitates were dried in a 60 °C oven overnight to obtain CuPMo@ZIF-67, FePMo@ZIF-67, NiPMo@ZIF-67, and ZnPMo@ZIF-67, respectively.

To prepare Ni_xCo_y@PZ, the Ni²⁺/Co²⁺ ratio was modified during the preparation of NiPMo@ZIF-67. The amounts of 0.6 mM nickel nitrate and 1.9 mM cobalt nitrate, 1.25 mM nickel nitrate and 1.25 mM cobalt nitrate, 1.9 mM nickel nitrate and 0.6 mM cobalt nitrate, and 2.5 mM nickel nitrate were dissolved in 25 mL methanol solution, respectively to obtain Ni₁Co₃@PZ, Ni₂Co₂@PZ, Ni₃Co₁@PZ, and Ni@PZ, respectively.

3.3.2. Preparation of T-XPMo@ZIF-67 and Ni_xCo_y@T-PZ

XPMo@ZIF-67 was placed into the Muffle furnace and slowly heated to 500 °C for 2 h. After it cooled down to room temperature, the synthesized products were washed with ethyl alcohol, and the precipitates were dried in a 60 °C oven to obtain T-NiPMo@ZIF-67, T-CuPMo@ZIF-67, T-FePMo@ZIF-67, T-ZnPMo@ZIF-67, respectively. The whole procedure of the preparation of T-NiPMo@ZIF-67, as well as the schematic diagram, were depicted in Figure 9a,b, respectively.

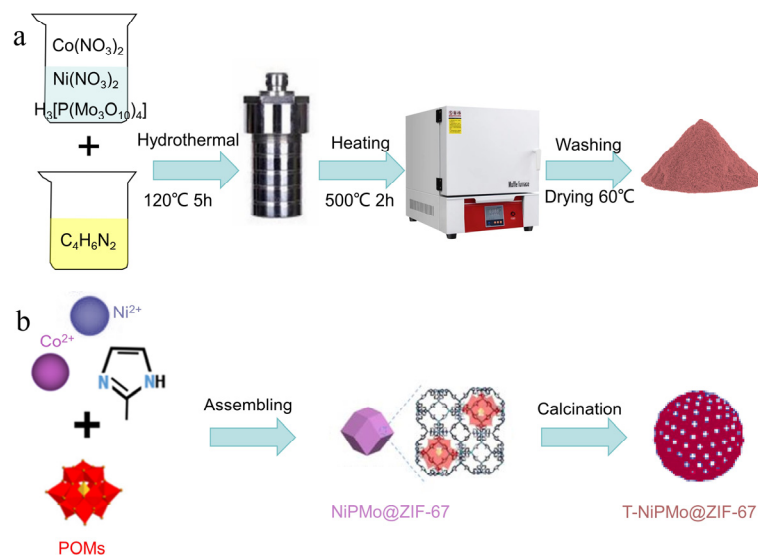


Figure 9. (a) The flow chart of the preparation of T-NiPMo@ZIF-67; (b) The schematic diagram of the preparation of T-NiPMo@ZIF-67.

Ni_xCo_y@T-PZ was prepared using the same procedure from Ni_xCo_y@PZ, and was denoted as Ni₁Co₃@T-PZ, Ni₂Co₂@T-PZ, Ni₃Co₁@T-PZ, and Ni@T-PZ, respectively.

3.3.3. Preparation of T-XPMo@ZIF-67 and Ni_xCo_y@PZ Modified Anode

The T-XPMo@ZIF-67 and Ni_xCo_y@PZ modified anodes were prepared by rolling method as previously described [23]. The detail procedure is as follows:

- (1) An amount of 0.5 g of activated carbon was mixed with T-XPMo@ZIF-67/Ni_xCo_y@PZ in a ratio of 1:0.01~1:0.05 by using anhydrous ethanol as solvent. The obtained mixture was placed in an ultrasonic cleaner with ultrasonic shaking and constant stirring for 40 min;
- (2) An amount of 0.25 g PTFE emulsion (60 wt%) was slowly added, and stirred continuously for 40 min;
- (3) The mixture was placed in a thermostatic water bath at 70 °C, and stirred continuously;
- (4) The catalyst modified anode with a thickness of 2~4 mm was obtained by rolling the mixture onto a Ni foam disc (diameter: 36 mm).

The blank control anode was prepared by using the same procedure with 0.5 g activated carbon powder.

3.4. Experimental Methods

The fuel cell was mainly made of polymethyl methylbenzoate (PMMA), with carbon cloth and nickel foam seals at both ends as the cathode and anode. An amount of 10 mL of 1 M glucose in 3 M KOH solution was used as substrate. The water used in the experiment was deionized water. A three-electrode system was employed in the electrochemical experiment. The reference electrode was saturated HgO electrode, the counter electrode was carbon cloth, and the working electrode was catalyst modified activated carbon/nickel foam. For the characterization of whole-cell performance (polarization curves and power density curves of the fuel cell), the fuel cell was assembled with a Ni_xCo_y@T-PZ doped anode and an active carbon air-cathode [44,45]. When placing the air cathode, we made sure that the catalytic layer of the air cathode faced the inner cavity of the fuel cell. The catalyst modified anode and the air cathode were pressed tightly with the rubber gasket to make them fully in contact with the nickel wire. After assembling the fuel cell, we checked whether there was water leakage and air tightness. Then, the glucose and KOH were injected into the inner cavity of the fuel cell from the inlet port on the side of the fuel cell, and the nitrogen was quickly vented for 10 min, so that the residual oxygen in the fuel cell chamber was discharged. The outlet was water-sealed during the exhaust process, and continuous small bubbles could be observed. After passing nitrogen, we sealed the air inlet and outlet of the fuel cell to prevent oxygen in the air from entering the fuel cell directly through these two ports. The temperature of the test environment was 23 °C ± 2 °C. The change of fuel cell voltage was measured in real time, and various electrochemical parameters were measured when the open circuit voltage was stable.

4. Conclusions

In this paper, a series of efficient catalysts for glucose oxidation were prepared by doping transitional metals into nanohybrids of PMo and ZIF-67. The doping of Ni²⁺ could significantly improve the electrochemical performance of T-PMo@ZIF-67. Among them, Ni₂Co₂@T-PZ showed the best performance. The maximum power density of the glucose cell doped with Ni₂Co₂@T-PZ catalyst reached 34.065 W m⁻², which was much higher than that of conventional cobalt-molybdenum-nickel oxides. The characterization results by SEM, XPS, and XRD indicate that Ni₂Co₂@T-PZ is a nanohybrid, being composed of Co₃O₄, CoMoO₄, CoNiO₄, and MoNiO₄. Ni₂Co₂@T-PZ maintains the hollow structure of ZIF-67, and there is a synergistic effect between Co²⁺, Ni²⁺, and Mo⁶⁺ for glucose oxidation. This work has considerable application prospects in the field of electrochemistry.

Supplementary Materials: The following supporting information can be downloaded at: <https://www.mdpi.com/article/10.3390/catal14010019/s1>. Figure S1: Equivalent circuit diagram; Figure S2: EDS image of Ni₂Co₂@T-PZ.

Author Contributions: Writing—original draft preparation, S.J. and N.K.; methodology, Y.Z. and Y.L.; data curation, M.L. and B.M.; conceptualization, N.K., X.Z. and X.L.; writing—review and editing, P.Z. and X.L. All authors have read and agreed to the published version of the manuscript.

Funding: This work was partially financially supported by the National Natural Science Foundation of China (No. 42377380) and the National Key R&D Program of China (Grant No. 2019YFC1407800).

Data Availability Statement: The data presented in this study are available on request from the corresponding author.

Conflicts of Interest: Authors have no conflict of interest to declare.

References

1. Li, B.; Wen, H.-M.; Cui, Y.; Zhou, W.; Qian, G.; Chen, B. Emerging Multifunctional Metal-Organic Framework Materials. *Adv. Mater.* **2016**, *28*, 8819–8860. [[CrossRef](#)] [[PubMed](#)]
2. Liu, D.; Wan, J.; Pang, G.; Tang, Z. Hollow Metal-Organic Framework Micro/Nanostructures and their Derivatives: Emerging Multifunctional Materials. *Adv. Mater.* **2019**, *31*, 1803291. [[CrossRef](#)] [[PubMed](#)]
3. Zhu, L.; Liu, X.-Q.; Jiang, H.-L.; Sun, L.-B. Metal-Organic Frameworks for Heterogeneous Basic Catalysis. *Chem. Rev.* **2017**, *117*, 8129–8176. [[CrossRef](#)] [[PubMed](#)]
4. Singh, R.; Singh, G.; George, N.; Singh, G.; Gupta, S.; Singh, H.; Kaur, G.; Singh, J. Copper-Based Metal-Organic Frameworks (MOFs) as an Emerging Catalytic Framework for Click Chemistry. *Catalysts* **2023**, *13*, 130. [[CrossRef](#)]
5. Kang, Y.-S.; Lu, Y.; Chen, K.; Zhao, Y.; Wang, P.; Sun, W.-Y. Metal-organic frameworks with catalytic centers: From synthesis to catalytic application. *Coordin. Chem. Rev.* **2019**, *378*, 262–280. [[CrossRef](#)]
6. Zhang, H.; Osgood, H.; Xie, X.; Shao, Y.; Wu, G. Engineering nanostructures of PGM-free oxygen-reduction catalysts using metal-organic frameworks. *Nano Energy* **2017**, *31*, 331–350. [[CrossRef](#)]
7. Liu, Y.; Zhao, P.; Duan, C.; He, C. Three-Dimensional Neodymium Metal-Organic Framework for Catalyzing the Cyanosilylation of Aldehyde and the Synthesis of 2,3-Dihydroquinazolin-4(1H)-one Derivatives. *Inorg. Chem.* **2023**, *62*, 10359–10368. [[CrossRef](#)]
8. Zhang, J.; Huang, Y.; Li, G.; Wei, Y. Recent Recent advances in alkoxylation chemistry of polyoxometalates: From synthetic strategies, structural overviews to functional applications. *Coordin. Chem. Rev.* **2019**, *378*, 395–414. [[CrossRef](#)]
9. Liu, J.-X.; Zhang, X.-B.; Li, Y.-L.; Huang, S.-L.; Yang, G.-Y. Polyoxometalate functionalized architectures. *Coordin. Chem. Rev.* **2020**, *414*, 213260. [[CrossRef](#)]
10. Gumerova, N.I.; Rompel, A. Synthesis, structures and applications of electron-rich polyoxometalates. *Nat. Rev. Chem.* **2018**, *2*, 0112. [[CrossRef](#)]
11. Zhang, Z.; Ma, X.; Han, X.; Cui, H.; Lu, Y.; Liu, S.; Liu, Y. Straightforward construction of hollow polyoxometalate-based metal-organic framework via pseudo-homoepitaxial growth. *Sci. China Chem.* **2022**, *65*, 1921–1928. [[CrossRef](#)]
12. Yang, H.; Li, J.; Zhang, H.; Lv, Y.; Gao, S. Facile synthesis of POM@MOF embedded in SBA-15 as a steady catalyst for the hydroxylation of benzene. *Micropor. Mesopor. Mat.* **2014**, *195*, 87–91. [[CrossRef](#)]
13. Du, D.-Y.; Qin, J.-S.; Li, S.-L.; Su, Z.-M.; Lan, Y.-Q. Recent advances in porous polyoxometalate-based metal-organic framework materials. *Chem. Soc. Rev.* **2014**, *43*, 4615–4632. [[CrossRef](#)] [[PubMed](#)]
14. Mialane, P.; Mellot-Draznieks, C.; Gairola, P.; Duguet, M.; Benseghir, Y.; Oms, O.; Dolbecq, A. Heterogenisation of polyoxometalates and other metal-based complexes in metal-organic frameworks: From synthesis to characterisation and applications in catalysis. *Chem. Soc. Rev.* **2021**, *50*, 6152–6220. [[CrossRef](#)] [[PubMed](#)]
15. Sun, J.; Abednatanzi, S.; Van Der Voort, P.; Liu, Y.-Y.; Leus, K. POM@MOF Hybrids: Synthesis and Applications. *Catalysts* **2020**, *10*, 578. [[CrossRef](#)]
16. Freire, C.; Fernandes, D.M.; Nunes, M.; Abdelkader, V.K. POM & MOF-based Electrocatalysts for Energy-related Reactions. *Chemcatchem* **2018**, *10*, 1703–1730.
17. Liu, J.; Huang, M.; Hua, Z.; Dong, Y.; Feng, Z.; Sun, T.; Chen, C. Polyoxometalate-Based Metal Organic Frameworks: Recent Advances and Challenges. *ChemistrySelect* **2022**, *7*, e202200546. [[CrossRef](#)]
18. Tiba, S.; Omri, A. Literature survey on the relationships between energy, environment and economic growth. *Renew. Sust. Energy Rev.* **2017**, *69*, 1129–1146. [[CrossRef](#)]
19. Nathaniel, S.P.; Adeleye, N. Environmental preservation amidst carbon emissions, energy consumption, and urbanization in selected african countries: Implication for sustainability. *J. Clean. Prod.* **2021**, *285*, 125409. [[CrossRef](#)]
20. Ehsanullah, S.; Quyen Ha, T.; Sadiq, M.; Bashir, S.; Mohsin, M.; Iram, R. How energy insecurity leads to energy poverty? Do environmental consideration and climate change concerns matters. *Environ. Sci. Pollut. Res.* **2021**, *28*, 55041–55052. [[CrossRef](#)]
21. Wang, J.; Zhang, X.; Li, Y.; Liu, P.; Chen, X.; Zhang, P.; Wang, Z.; Liu, X. Sweet Drinks as Fuels for an Alkaline Fuel Cell with Nonprecious Catalysts. *Energies* **2021**, *14*, 206. [[CrossRef](#)]
22. Liu, T. Glucose Fuel Cells and Membranes: A Brief Overview and Literature Analysis. *Sustainability* **2022**, *14*, 8376. [[CrossRef](#)]
23. Kerzenmacher, S.; Ducree, J.; Zengerle, R.; von Stetten, F. Energy harvesting by implantable abiotically catalyzed glucose fuel cells. *J. Power Sources* **2008**, *182*, 1–17. [[CrossRef](#)]
24. Antolini, E. External abiotic glucose fuel cells. *Sustain. Energy Fuels* **2021**, *5*, 5038–5060. [[CrossRef](#)]
25. Do, U.P.; Seland, F.; Johannessen, E.A. A micro fuel cell for abiotical catalysis of glucose. *J. Power Sources* **2020**, *478*, 229032. [[CrossRef](#)]
26. Ho, J.; Li, Y.; Dai, Y.; Kim, T.; Wang, J.; Ren, J.; Yun, H.; Liu, X. Ionothermal synthesis of N-doped carbon supported CoMn₂O₄ nanoparticles as ORR catalyst in direct glucose alkaline fuel cell. *Int. J. Hydrogen Energy* **2021**, *46*, 20503–20515. [[CrossRef](#)]

27. Huang, J.; Simons, P.; Sunada, Y.; Rupp, J.L.M.; Yagi, S. Pt-Catalyzed D-Glucose Oxidation Reactions for Glucose Fuel Cells. *J. Electrochem. Soc.* **2021**, *168*, 064511. [[CrossRef](#)]
28. Dong, F.; Liu, X.; Irfan, M.; Yang, L.; Li, S.; Ding, J.; Li, Y.; Khan, I.U.; Zhang, P. Macaroon-like FeCo₂O₄ modified activated carbon anode for enhancing power generation in direct glucose fuel cell. *Int. J. Hydrogen Energy* **2019**, *44*, 8178–8187. [[CrossRef](#)]
29. Zhao, Y.; Liu, X.; Wang, X.; Zhang, P.; Shi, J. Peony petal-like 3D graphene-nickel oxide nanocomposite decorated nickel foam as high-performance electrocatalyst for direct glucose alkaline fuel cell. *Int. J. Hydrogen Energy* **2017**, *42*, 29863–29873. [[CrossRef](#)]
30. Irfan, M.; Liu, X.; Li, S.; Khan, I.U.; Li, Y.; Wang, J.; Wang, X.; Du, X.; Wang, G.; Zhang, P. High-performance glucose fuel cell with bimetallic Ni-Co composite anchored on reduced graphene oxide as anode catalyst. *Renew Energy* **2020**, *155*, 1118–1126. [[CrossRef](#)]
31. Yang, L.; Liu, X.; Ding, J.; Li, S.; Dong, F.; Irfan, M.; Li, Y.; Wang, G.; Du, X.; Zhang, P. Chlorella-derived porous heteroatom-doped carbons as robust catalysts for oxygen reduction reaction in direct glucose alkaline fuel cell. *Int. J. Hydrogen Energy* **2019**, *44*, 2823–2831. [[CrossRef](#)]
32. Li, Y.; Dong, F.; Jiao, S.; Wang, J.; Dai, Y.; Irfan, M.; Liu, X. Co²⁺-P(W₃O₁₀)₄(³⁻) modified activated carbon as an efficient anode catalyst for direct glucose alkaline fuel cell. *Int. J. Hydrogen Energy* **2022**, *47*, 22952–22962. [[CrossRef](#)]
33. Akhairi, M.A.F.; Kamarudin, S.K. Catalysts in direct ethanol fuel cell (DEFC): An overview. *Int. J. Hydrogen Energy* **2016**, *41*, 4214–4228. [[CrossRef](#)]
34. Din, M.A.U.; Idrees, M.; Jamil, S.; Irfan, S.; Nazir, G.; Mudassir, M.A.; Saleem, M.S.; Batool, S.; Cheng, N.; Saidur, R. Advances and challenges of methanol-tolerant oxygen reduction reaction electrocatalysts for the direct methanol fuel cell. *J. Energy Chem.* **2023**, *77*, 499–513. [[CrossRef](#)]
35. Gong, L.; Yang, Z.; Li, K.; Xing, W.; Liu, C.; Ge, J. Recent development of methanol electrooxidation catalysts for direct methanol fuel cell. *J. Energy Chem.* **2018**, *27*, 1618–1628. [[CrossRef](#)]
36. Onescu, V.; Erickson, D. High volumetric power density, non-enzymatic, glucose fuel cells. *Sci. Rep.* **2013**, *3*, 1226. [[CrossRef](#)] [[PubMed](#)]
37. Simons, P.; Schenk, S.A.; Gysel, M.A.; Olbrich, L.F.; Rupp, J.L.M. A Ceramic-Electrolyte Glucose Fuel Cell for Implantable Electronics. *Adv. Mater.* **2022**, *34*, 2109075. [[CrossRef](#)]
38. Su, C.-H.; Sun, C.-L.; Peng, S.-Y.; Wu, J.-J.; Huang, Y.-H.; Liao, Y.-C. High performance non-enzymatic graphene-based glucose fuel cell operated under moderate temperatures and a neutral solution. *J. Taiwan Inst. Chem. E* **2019**, *95*, 48–54. [[CrossRef](#)]
39. Guo, H.; Yin, H.; Yan, X.; Shi, S.; Yu, Q.; Cao, Z.; Li, J. Pt-Bi decorated nanoporous gold for high performance direct glucose fuel cell. *Sci. Rep.* **2016**, *6*, 39162. [[CrossRef](#)]
40. Lv, Z.; Zhong, Q.; Bu, Y. Controllable synthesis of Ni-Co nanosheets covered hollow box via altering the concentration of nitrate for high performance supercapacitor. *Electrochim. Acta* **2016**, *215*, 500–505. [[CrossRef](#)]
41. Liu, H.; Jin, M.; Zhan, D.; Wang, J.; Cai, X.; Qiu, Y.; Lai, L. Stacking faults triggered strain engineering of ZIF-67 derived Ni-Co bimetal phosphide for enhanced overall water splitting. *Appl. Catal. B-Environ.* **2020**, *272*, 118951. [[CrossRef](#)]
42. Guo, G.; Li, W.; Ahmed, T.; Hu, D.; Cui, R.; Zhang, B.; Zhang, X. Production of liquid fuels from Kraft lignin over bimetallic Ni-Mo supported on ZIF-derived porous carbon catalyst. *RSC Adv.* **2021**, *11*, 37932–37941. [[CrossRef](#)] [[PubMed](#)]
43. Yang, X.-L.; Ye, Y.-S.; Wang, Z.-M.; Zhang, Z.-H.; Zhao, Y.-L.; Yang, F.; Zhu, Z.-Y.; Wei, T. POM-Based MOF-Derived Co₃O₄/CoMoO₄Nanohybrids as Anodes for High-Performance Lithium-Ion Batteries. *ACS Omega* **2020**, *5*, 26230–26236. [[CrossRef](#)] [[PubMed](#)]
44. Gao, M.; Liu, X.; Irfan, M.; Shi, J.; Wang, X.; Zhang, P. Nickel-cobalt composite catalyst-modified activated carbon anode for direct glucose alkaline fuel cell. *Int. J. Hydrogen Energy* **2018**, *43*, 1805–1815. [[CrossRef](#)]
45. Irfan, M.; Khan, I.U.; Wang, J.; Li, Y.; Liu, X. 3D porous nanostructured Ni₃N-Co₃N as a robust electrode material for glucose fuel cell. *RSC Adv.* **2020**, *10*, 6444–6451. [[CrossRef](#)] [[PubMed](#)]
46. Wang, Y.; Wang, Y.; Zhang, L.; Liu, C.-S.; Pang, H. Core-shell-type ZIF-8@ZIF-67@POM hybrids as efficient electrocatalysts for the oxygen evolution reaction. *Inorg. Chem. Front.* **2019**, *6*, 2514–2520. [[CrossRef](#)]
47. Abdelkader-Fernandez, V.K.; Fernandes, D.M.; Balula, S.S.; Cunha-Silva, L.; Freire, C. Oxygen Evolution Reaction Electrocatalytic Improvement in POM@ZIF Nanocomposites: A Bidirectional Synergistic Effect. *ACS Appl. Energy Mater.* **2020**, *3*, 2925–2934. [[CrossRef](#)]
48. Tang, Y.; Zou, Z.; Wu, X.; Zuo, P.; Wang, L.; Huang, G.; Zhu, J.; Zhong, S. ZIF-67@POM hybrid-derived unique willow-shaped two-dimensional Mo-CoP nanostructures as efficient electrocatalysts for the oxygen evolution reaction. *New J. Chem.* **2023**, *47*, 9887–9893. [[CrossRef](#)]
49. Abdelkader-Fernandez, V.K.; Fernandes, D.M.; Balula, S.S.; Cunha-Silva, L.; Freire, C. Advanced framework-modified POM@ZIF-67 nanocomposites as enhanced oxygen evolution reaction electrocatalysts. *J. Mater. Chem. A* **2020**, *8*, 13509–13521. [[CrossRef](#)]

Disclaimer/Publisher's Note: The statements, opinions and data contained in all publications are solely those of the individual author(s) and contributor(s) and not of MDPI and/or the editor(s). MDPI and/or the editor(s) disclaim responsibility for any injury to people or property resulting from any ideas, methods, instructions or products referred to in the content.